Characterization of surface finiture of different steels on mechanical components for energy harvesting

Elisa Destefano, Andrea Giura, Luigi Ribotta

Characterization of surface finiture of different steels on mechanical components for energy harvesting

T.R. 16/2024 June 2024

I.N.RI.M. TECHNICAL REPORT

Contents

Abstract

Erosion of wind turbines can reduce performance and lead to 3-5% power losses, with costly repairs and replacements, particularly offshore. To minimize these costs, it's crucial to characterize the durability of different materials. This study focuses on correlating surface roughness and geometry of specific wind turbine components with their functionalities. the surface, which interacts with the external environment, is critical, and its topography must be considered. Surface roughness significantly influences the overall efficiency, making its evaluation essential and it becomes important to evaluate it in accordance with established standards. The International Organization for Standardization (ISO) provides guidelines to ensure uniformity and accuracy in surface roughness measurements. Different techniques are available and can be categorized as contact and non-contact methods. Contact-based methods, such as the stylus profilometer, involves physical contact between the probe and the specimen's surface, offering high resolution analysis. On the other side, non-contact methods, such as optical profilometer and the chromatic confocal punctual sensor (CCPS), operate without direct contact with the surface, minimizing the risk of damage. Different mechanical components with distinct surface treatments were analyzed to determine their roughness and dimensional parameters. Their analysis aims to understand the relationship between surface properties, functionality, and overall efficiency in energy harvesting systems.

L'erosione delle turbine eoliche può ridurre le prestazioni e portare a perdite di potenza del 3-5%, con costose riparazioni e sostituzioni, soprattutto in mare aperto. Per ridurre al minimo questi costi, è fondamentale caratterizzare la durata dei diversi materiali. Questo studio si concentra sulla correlazione tra la rugosità superficiale e la geometria di specifici componenti di turbine eoliche e le loro funzionalità. La superficie, che interagisce con l'ambiente esterno, è fondamentale e occorre considerare la sua topografia. La rugosità della superficie influenza in modo significativo l'efficienza complessiva, rendendo essenziale la sua valutazione e diventa importante valutarla in base a standard consolidati. L'Organizzazione Internazionale per la Standardizzazione (ISO) fornisce linee guida per garantire l'uniformità e l'accuratezza delle misurazioni della rugosità superficiale. Sono disponibili diverse tecniche che possono essere classificate come metodi a contatto e non a contatto. I metodi a contatto, come il profilometro a stilo, prevedono il contatto fisico tra la sonda e la superficie del campione, offrendo un'analisi ad alta risoluzione. Dall'altro lato, i metodi senza contatto, come il profilometro ottico e il sensore puntuale confocale cromatico (CCPS), operano senza contatto diretto con la superficie, riducendo al minimo il rischio di danni. La loro analisi mira a comprendere la relazione tra proprietà della superficie, funzionalità ed efficienza complessiva nei sistemi di raccolta dell'energia.

Introduction

The surface is defined as the boundary of a component interacting with the external environment, and it is important to consider its topography and material characteristics of the object under investigation. The characterization of surface topography is a branch of metrology that includes a large range of parameters. Surface roughness is a critical factor to consider while analyzing mechanical components for energy harvesting systems, particularly in wind turbines, as it significantly influences the overall efficiency. The presence of surface imperfections can manifest in several ways, each with detrimental effects. For instance, micropitting is caused by impurities on the surface that can create microdamages. Similarly, macropitting occurs when the contact stress of the surface increases and becomes a challenge for the structure's integrity. Moreover, wear and other detrimental effects can influence the roughness.

Given the significance of surface roughness in energy harvesting systems, it becomes important to evaluate it in accordance with established standards. The International Organization for Standardization (ISO) is a worldwide federation of national standards bodies, and its scope is to develop and publish international standards in order to enable industry competitiveness, product functionality and compatibility, and ensuring the safety and quality of products and services. Within the framework of the Geometrical Product Specification (GPS) system used to define the geometrical requirements of workpieces in engineering specifications, and the requirements for their verification, guidelines to ensure uniformity and accuracy in roughness measurements have been developed, namely ISO 21920:2022 (Surface texture: Profile).

Different techniques are available and can be categorized as contact and non-contact methods. In this study, I used and compared both these types of techniques. Contact-based methods, such as the stylus profilometer, involve physical contact between the probe and the sample's surface, offering high resolution analysis. On the other side, non-contact methods, such as optical profilometer (confocal and interferometric modes) and the chromatic confocal punctual sensor (CCPS), operate without a direct contact with the surface, minimizing the risk of damage.

Analyzing the surface roughness can be sometimes challenging because it can be easily influenced by the evaluation length or filters that are applied. In conclusion, this study aims to provide insights into the surface characteristics of mechanical components for energy harvesting systems, contributing to the enhancement of their performance and durability.

1. ANALYSIS TECHNIQUES

1.1. STYLUS PROFILOMETER

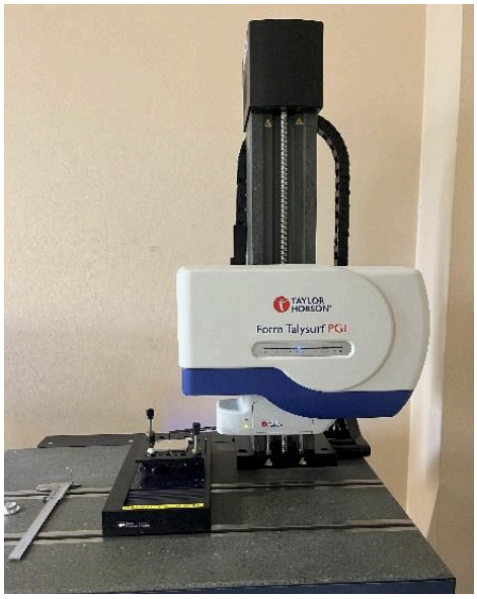

Figure 1: TAYLOR HOBSON FORM TALYSURF PGI NOVUS S10 stylus profilometer.

The form TalySurf PGI 10 NOVUS (Figure 1) is the most advanced system for 3D measurement, and contour analysis, angle and diameter detection, and surface finiture. With a stylus profilometer, the measurement of a surface is made by traversing a conical stylus tip over a line, allowing both profile and step height to be analyzed quantitatively. Surface profile measurement is achieved by measuring a line across the surface and representing that line as a height function with lateral displacement, permitting the measurement of surface characteristics of different devices thanks to the high precision of this stylus profilometer. Step height measurements (from 5 nm to 800 μm) are performed in a robust and reliable way thanks to the instrument high resolution (down to 0.2 nm) and high repeatability, ensured by high electronic stability, anti-vibration table [1].

1.2. OPTICAL PROFILOMETER

Figure 2: SENSOFAR PLμ2300 optical profilometer.

Optical profilometers (Figure 2) offer versatile solutions for 3D surface analysis, with two operational modes: confocal and interferometric. While the resolution in Z axis depends on the operational mode used, the resolution in X and Y axes ranges from 0.2 μm to 1 μm, depending on pixel size, objective used and optical resolution due to Abbe diffraction limit. Using an optical instrument, a profile can be extracted from an areal measurement [2].

1.2.1. CONFOCAL MODE

Confocal microscopy sets itself apart from standard light microscopy through the use of confocal apertures that ensure only light at the point of focus on the test surface enters the detector.

To build up a 3D image the sample or the objective is scanned vertically such that each point on the sample surface passes through the focal plane of the microscope, so multiple optical sections along the Z direction are done. The signal collected at a single point on the object during a vertical scan is evaluated for maximum irradiance, that corresponds to the imaged point being in focus (Figure 3)

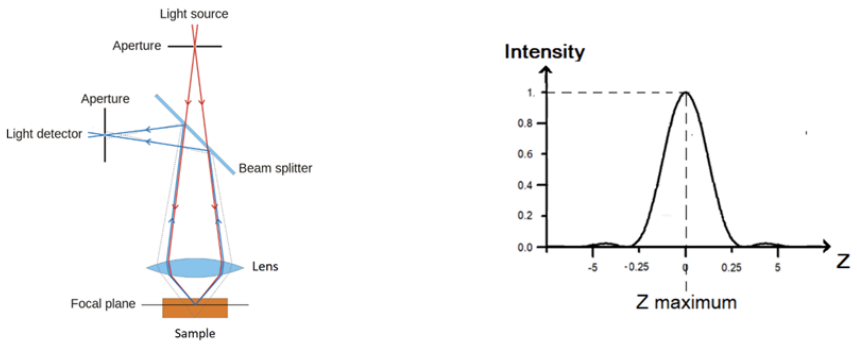

Figure 3: Principle of confocal profilometer.

Confocal microscopy provides a wide range of applications either for flat and rough surfaces, various materials and reflectivity, while the main disadvantage is that the signal decreases and becomes unreliable for high surface slope.

1.2.2. INTERFEROMETRIC MODE

Interferometric profilometers use interference patterns to generate precise 3D representations of the surface. The main concept is the interferometer, which is an optical device capable of dividing the beam of light from a specific source into two different beams and then recombining them to create an interference pattern, which can be studied to understand the difference in paths.

The light, from the source, is divided into two beams because of the presence of a beamsplitter. One beam is reflected from the "reference mirror" and the other from the sample, but at the end, these two beams are recombined together by the beamsplitter and interfere, creating a "fringe pattern" (Figure 4).

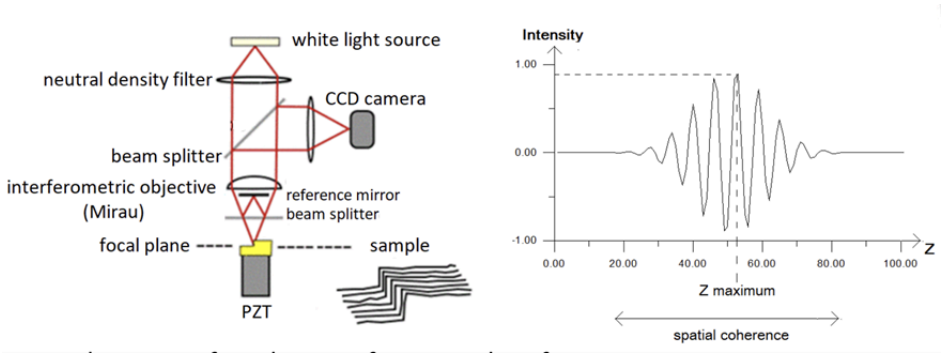

Figure 4: Principle of CSI interferometric profilometer.

We have two operating modes for interferometric profilometer: CSI (coherence scanning interferometry, with resolution in Z axis (1nm)) or PSI (phase-shifting interferometry; used for super smooth surfaces (resolution in Z axis (0.1nm)), both of them offer high surface area coverage and analysis.

Coherent scanning interferometry (CSI) allows to measure flat samples, rough surfaces and high steps. The interferometric objective moves vertically to scan the surface at varying heights. As the system scans upward, the maximum of the envelope of the fringe within its coherence length for each pixel of the image. Finally, by the vertical position corresponding to the maximum of the fringe envelope at each pixel the surface morphology is reconstructed.

Phase shifting interferometry (PSI) collects intensity data from every point of the CCD image sensor. During the measurement, a piezoelectric transducer (PZT) linearly moves the reference surface or the objective of a small, known amount to cause a phase shift between the test and reference beams. The system records the intensity of the resulting interference pattern at many

different relative phase shifts, and then converts the intensity to wave front (phase) data by integrating the intensity data.

Despite their high resolution, interferometric systems are costlier and require more setup and acquisition time than confocal and stylus profilometer.

1.3. CCPS: CHROMATIC CONFOCAL POINT SENSOR

The Chromatic Confocal Point Sensor (CCPS) (Figure 5) is able to carry out optical thickness measurement and optical distance measurement at high speeds and with optimal precision for a variety of industrial surfaces, which might be reflecting or dispersive, opaque or transparent, rough or polished.

Figure 5: CCPS, Precitec CHRicidile 2S.

The chromatic confocal point sensor takes advantage from a lens error commonly known as chromatic aberration: the axial position of the focal point of an uncorrected lens depends on the color (wavelength) of the light to be focused. Depending on the distance of the target from the focusing lens, light of just a very small wavelength region is focused on the target's surface; all other spectral components of the light source are illuminating a much wider area of the surface.

The focusing lens is also used to receive the backscattered light from the target's surface and to focus it into an optical fiber (Figure 6)

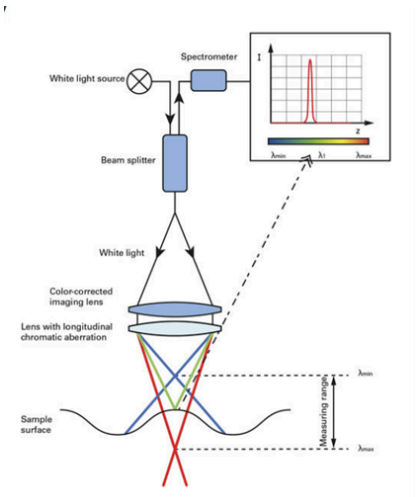

Figure 6: Principle of the CCPS.

Incident white light is imaged through a chromatic lens to emit monochromatic light along the z-axis, when an object is present in this color field, a single wavelength is fixed to its surface and then reflected back to the optical system. The backscattered beam passes through a filtering pinhole and is then acquired by a spectrometer. The beam's specific wavelength is calculated to precisely determine the position of the surface in the measurement field.

2. CASE STUDIES

Erosion of wind turbines can reduce performance and lead to 3-5% power losses [3]. Repairs and replacements, particularly for offshore environments, can be costly. Therefore, it is important to characterize the durability of different materials to minimize the need for repair or replacement.

In this study, the focus is correlating surface roughness and geometry of specific components of wind turbines with their functionalities, in order to understand how different machining processes affect the performance [4].

2.1. GEAR TOOTH

Gears are crucial components of wind turbine transmission systems, working by engaging the teeth of one specific gear with those of another in order to enable the transfer of rotational power. The surface roughness of the gears plays a key role: in fact, having a good surface significantly reduces (i) the frictional torque, (ii) the bulk temperature of the gear and (iii) acoustic noise, increasing the overall efficiency. In general, reducing the surface roughness would reduce the amount of damage and the initiation of cracks or other types of failure [5].

In wind turbine applications, gears are crafted from case-hardened steel and undergo soft cutting followed by heat treatment and a hard finishing process. The grinding process [6] is an abrasive material removal method used to refine gear surfaces to get desired specifications by using vitrified aluminum oxide wheels. In addition, the use of aluminum oxide provides enhanced durability and increased heat resistance, enabling precise material removal and ensuring efficiency and longevity of the workpiece [7].

Grinding reduces surface roughness by increasing the dimensional and geometric accuracy and can be used for both by metal and non-metal materials with different shapes and profiles. The process involves mainly two steps, *i.e.* the coating of the tool and the micro extrusion plastic deformation. The coating of the grinding tool's surface with abrasive material, in order to increase its hardness, which must be higher than the workpiece one; the micro extrusion plastic deformation allows to gradually obtain the final desired features by refining the workpiece. These cutting particles induce a cutting action on the workpiece's surface and cut a thin layer of metal from it. In the meantime, the pressure created on the surface will create a micro-extrusion plastic deformation. While using some particular abrasives, these could have a chemical effect, resulting in a thin oxide film that easily wears off.

The main advantages of using this technique are the high precision and accuracy that can be achieved, versatility, ability to machine hard materials, improved surface finish, avoids burr

formation, and limits heat generation. On the other hand, the disadvantages are the high cost of the equipment and maintenance, as well as the limited material removal rate compared to other faster techniques [8].

On the other hand, super-finishing [9], which employs controlled shot peening and isotropic finishing, refines the gear surfaces after grinding. Shot peening [10] is a cold working process for metal surfaces in which the substrate metal is bombarded with various media, called “shots”, producing some stresses and dislocations on the surface to improve its hardness. This compressive stress region may be several times greater than any imposed tensile stress, improves fatigue life and inhibits the crack propagation.

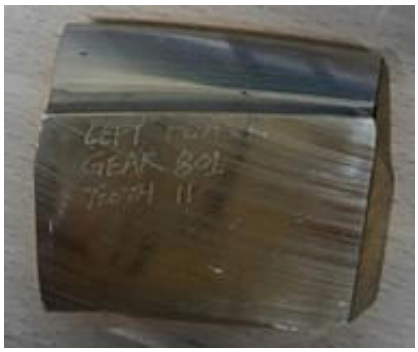

Figure 7: Gear tooth 801 produced by Newcastle University.

Figure 8: Gear tooth 825 produced by Newcastle University.

In this thesis, I studied two portions of gear teeth designed by University of Newcastle produced by grinding In this thesis, I studied two portions of gear teeth designed by University of Newcastle produced by grinding (gear 801 (Figure 7)) and shot peening (gear 825 (Figure 8)). The measurements were performed in two different directions to display and analyze how the surface processing influenced the final roughness of the sample (Figure 9 and Figure 10).

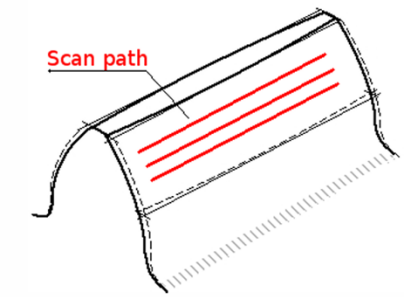

Figure 9: X direction path scans for gears.

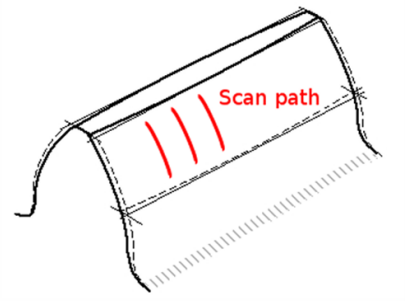

Figure 10: Y direction path scans for gears.

2.2. BALL BEARING

The material 1.3505 is classified as bearing steels and is used for wear-exposed parts in mechanical engineering and tools. Specifically engineered for rolling contact and fatigue resistance, its hardened nature endows it with exceptional hardness, strength, and cleanliness, which are essential for enduring high-stress cycles and fatigue.

Additionally, the 100Cr6 material is a construction steel of spheroidal bearing steel grade that exhibits high hardness, abrasion resistance, and friction resistance. It is mostly used for components subjected to high friction or pressure under moderate temperatures. Furthermore, this material has an extremely limited tendency to deform, medium hardening capacity, and may be tempered at 150° during friction [11, 12].

The use of these materials in ball bearing applications ensures longevity, reliability, and optimal performance, even under demanding operational conditions. Their superior properties make them indispensable for achieving smooth, efficient and durable mechanical systems (Figure 11).

The measurements in the ball bearing were performed in two different shown in Figure 12

Figure 11: Ball bearing produced by MG Marposs.

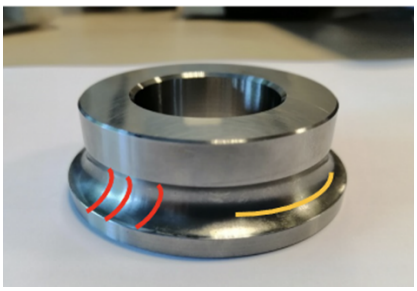

Figure 12: Measurement directions in ball bearing (red: torus, yellow: circle).

2.3. LARGE RING SECTION

The bearing under discussion is a portable ring segment with a circular groove in the axial direction, made of AISI 440C stainless steel [13]. To achieve a hardness over 60 HRC, it underwent milling, heat treatment, and precision grinding (Figure 13).

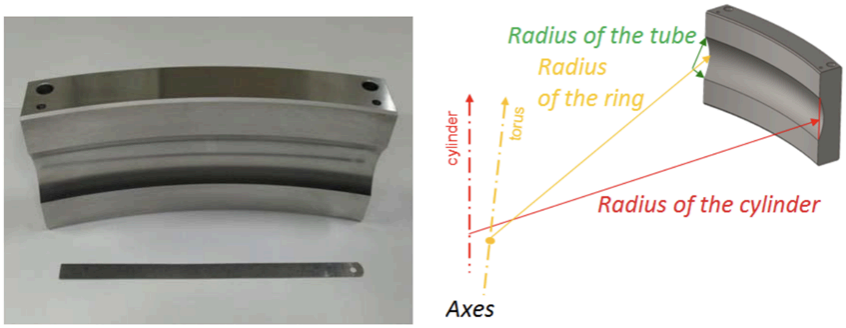

Figure 13: Large ring segment produced by MG Marposs, reported together with its form charactertistics.

Starting from an AISI 440 C (martensitic stainless steel with the highest carbon content) parallelepiped and by using a three axes vertical machining center (FADAL 3016 L) a pre-rough machining phase was made to obtain the ring segment complete of the torus profile with 2 mm machining allowance. Subsequently , the segment underwent a rigorous heat treatment process, including:

1) Solvent washing at 124°C for 15 minutes to clean the segment by removing any oils, grease or contaminants from the machining process, ensuring that the following heat treatments are effective.
2) Stabilization at 650°C for 120 minutes, in a protective atmosphere of a gaseous mixture of N2 (94%) and H2 (6%). This step was then followed by a oven cooling to 300°C, then still air to room temperature, to relieve internal stresses induced during machining, helping in preventing dimensional changes during hardening and subsequent processing.
3) Hardening in which a pre-heating at 760°C for 40 minutes was performed, then followed by a reheating at 1070°C for other 45 minutes in a protective atmosphere to prevent oxidation and decarburization to increase the hardness and strength of the steel. In fact, this step transforms the microstructure to martensite.
4) Cooling in a ventilated chamber for 60 minutes to lock in the hardened microstructure.
5) Double-cycle cooling at −100°C for 4 hours per cycle in order to enhance the wear resistance and dimensional stability by transforming retained austenite into martensite and relieving residual stresses.
6) Tempering which includes a first heating at 145°C for 5 hours (followed by natural cooling to 80°C) and a second heating at 145°C for other 5 hours (followed by natural cooling to room temperature). This process is conducted to reduce brittleness and to improve toughness by tempering the martensite, but also to stabilize the microstructure, ensuring the component to withstand operational stresses without failure.

Following heat treatment, reference holes were ground onto the top plane of the segment using a Cartesian coordinate grinding machine, serving as reference points for subsequent operations. Rough grinding of the cylindrical profile was also executed using the same machine. The final step involved the precision grinding of both the cylindrical and torus profiles. For the torus profile, a plunge grinding strategy with a spherical grindstone was employed under a coolant emulsion jet (water and oil mixture 8%) to mitigate thermal stress.

AISI 440C martensitic stainless steel has good corrosion resistance, high strength, hardness, and wear resistance when subjected to heat treatment. Its high carbon content, combined with Cr, Mo, and V, makes it ideal for applications requiring high wear resistance and moderate corrosion resistance. The main reason for the application of this material in wind turbines is not only because it has good corrosion resistance, which is useful since wind turbines are exposed

to harsh outdoor environments, but also because we have good wear resistance due to rotation and loads, high strength, and dimensional stability, useful for maintaining smooth operation and minimal vibration.

The measurements were performed in two different directions shown in Figure 14 and Figure 15.

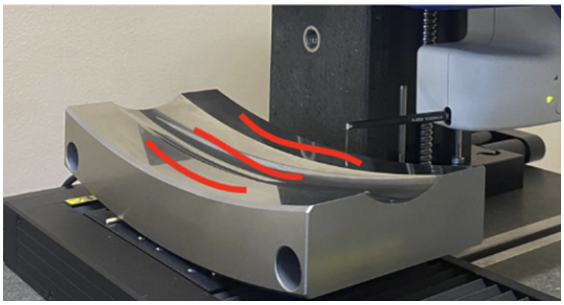

Figure 14: 0° degree large ring segment.

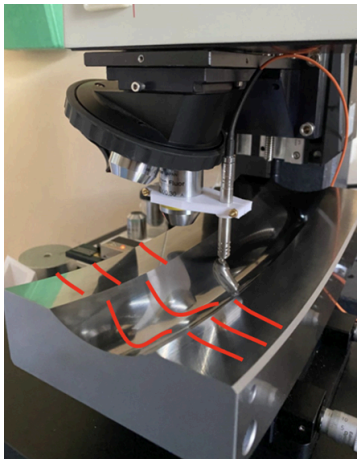

Figure 15: 90° degree large ring segment.

3. ROUGHNESS, WAVINESS AND FORM

It is important to understand the difference between roughness, waviness and form since most surfaces are the result of a combination of the effects of these three. [14]. The number of waves in the functional length also has some influence on how. we classify the irregularities: if we consider a single wave on a small surface, it can be considered as a curvature, but if we consider a larger number of waves on a larger surface area, then we can define it as waviness. It is important to separate roughness, waviness and form depending on their cause and on their performance factors. We can define them as follows:

- Roughness can be defined as the irregularities which are produced during the production process (e.g.: marks due to grinding or abrasion)
- Waviness is the part of the texture on which roughness is superimposed; it can be due to vibrations, work deflections and strains in the material. This is usually associated to the individual machine.
- Form is the general shape of the surface, ignoring variations due to roughness and waviness.

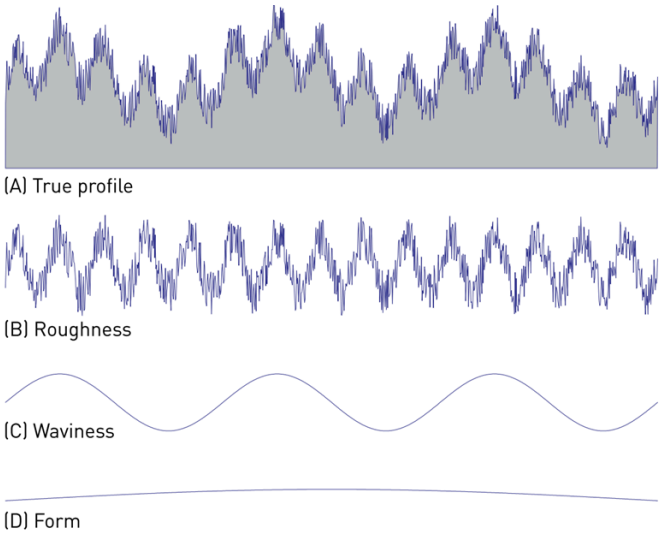

Figure 16: [A] combination of waviness, roughness and form, [B] roughness profile, [C] waviness profile, [D] form.

4. RESULTS

4.1. ROUGHNESS PARAMETERS

In my study, I used the metrological software "MountainsMap 10" to extract both, and extract both roughness parameters and geometry of the mechanical components analyzed. Rq, Rsk, Rku, Rz, Ra, Rk, Rpk, Rvk, Rmrk1, Rmrk2 parameters were extracted according to ISO 21920 by using a S-filter 300:1[1] "Gaussian[2] (ISO 16610-21)", F-operation "Least squares (LS) polynomial" (with degree 3 for gear teeth and degree 2 for all the other samples) and an L-filter 0.025 mm [15].

Filtration [16] plays a crucial role at multiple stages of surface texture analysis. For example, a morphological filter is frequently used to correct the impact of the stylus tip on raw data. When working with data from optical probes, an outlier removal filter might be necessary to clean the data. Moreover, to compare measurements obtained from different instruments, a smoothing filter such as a λs or S-Filter can be used. However, the primary reason for using a filter is typically to differentiate long-scale components from short-scale components, thereby separating waviness from roughness, and subsequently calculating parameters according to specific standards.

- The S-Filter removes short-scale components.
- The L-Filter removes long-scale components.
- The F-Operator is the form removal operation.

In particular, the parameters were extracted using the following procedure:

a) From optical profilometer we measure a topography of a surface; since from stylus profilometer we obtain a single profile, in order to build a surface, for some samples the "2D measurement" option was used. With this option, the stylus profilometer records different profiles on a specific area, which is combined to create a series of profiles (Figure 17). Since we want to compare different techniques (stylus, optical, CCPS) in a consistent way, few profiles were extracted from the surfaces to obtain the correct results [17].

[1] 300:1 should be adopted unless the cut-off selected does not have enough data points in its traverse length.

[2] half of the first sample length and half of the last sample length are discarded.

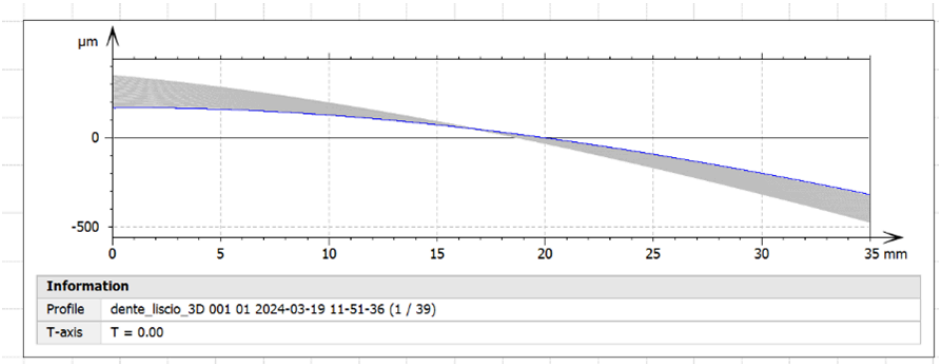

Figure 17: "create series" gear 801, X direction measured by stylus profilometer.

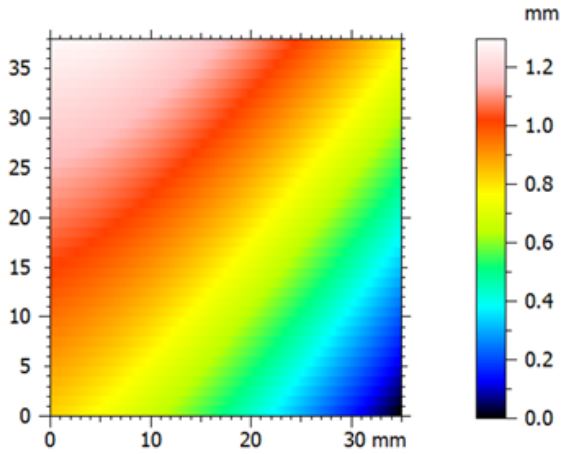

Figure 18: Surface gear 801, X direction measured by stylus profilometer.

b) In order to extract roughness parameters, the extracted profiles are filtered according to a Gaussian ISO 16610-21 with 300:1 S-filter: L-filter, a L-filter 0.025 mm and a form F-operation "Least squares (LS) polynomial" (with degree 2 or 3 depending on what component we are analyzing).

ISO 21920 - Roughness (S-L)			
S-filter (λs): Gaussian, 300:1 (0.8 µm)			
F: Form removed (LS-poly2)			
L-filter (λc): Gaussian, 0.25 mm			
Evaluation length: All λc (1)			
Height parameters			
Rq	1.34	µm	
Rsk	0.154		
Rku	8.10		
Rz	12.2	µm	*Average of values on: All λc (1)*
Ra	0.874	µm	
Functional (Rk) parameters			
Rk	1.69	µm	
Rpk	2.11	µm	
Rvk	2.04	µm	
Rmrk1	15.9	%	
Rmrk2	81.1	%	

Figure 19: Roughness parameters table from MountainsMap 10.

4.2. DIMENSIONAL PARAMETERS FOR GEAR TEETH

Another important step is the extraction of the polynomial coefficients , in order to know the mathematical function that describes the surface form of the teeth.

A polynomial fit of the second degree of a bivariate function involves fitting a quadratic polynomial to a set of data points in two dimensions. This type of polynomial model is expressed as:

$$f(x, y) = ax^2 + by^2 + cxy + dx + ey + f \tag{1}$$

where (x) and (y) are the independent variables, and (a, b, c, d, e, f) are the coefficients to be determined through the fitting process. By using a second-degree polynomial, the model can capture more complex relationships between the two variables compared to a linear fit. The quadratic terms allow for curvature in the fitted surface, enabling the model to better approximate the underlying behavior of the bivariate function.

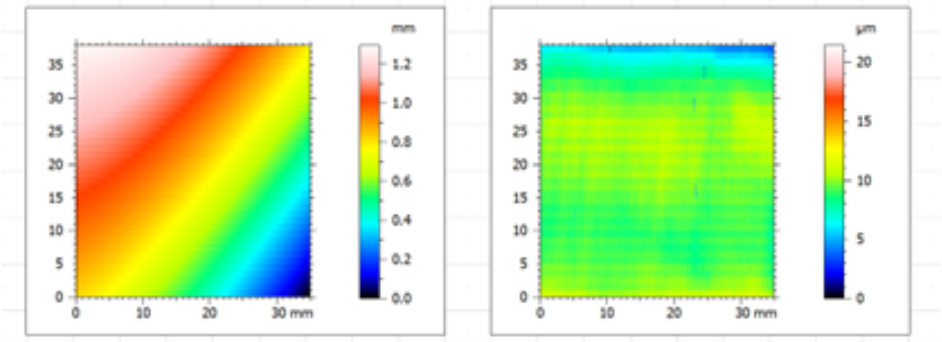

Figure 20: “Remove form” for obtaining polynomial coefficients.

4.3. ROUGHNESS PARAMETERS

The roughness parameters taken into account are the following [18–20]:

- Ra (arithmetic mean deviation) → represents the arithmetic mean of the absolute ordinate Z(x) within the sampling length. It is not significantly influenced by scratches, contamination, or measurement noise. It is very easy to define and provides valuable information on height variations without considering small changes in profile.

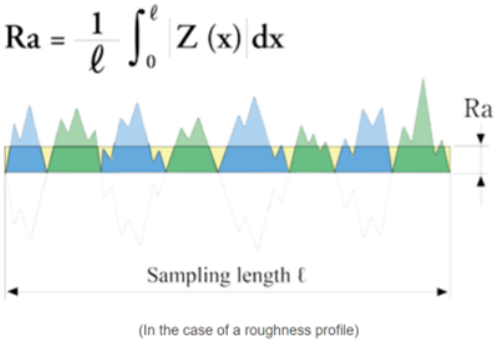

Figure 21: Ra parameter.

- Rq (root mean square deviation) → represents the root mean square for Z(x) within the sampling length. This parameter provides for easy statistical handling and enables stable results because is not significantly influenced by scratches, contamination, and measurement noise. It is generally more sensitive than Ra to large deviations from the mean line.

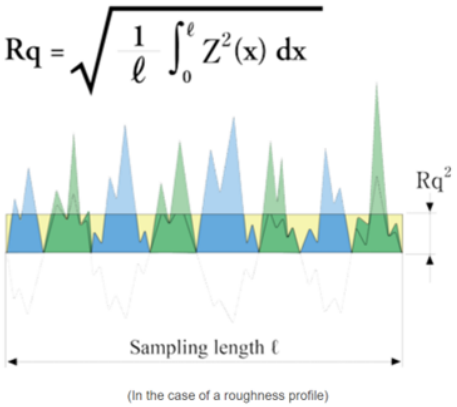

Figure 22: Rq parameter.

- Rz (maximum height) → represents the sum of the peak height Zp and the maximum valley depth Zv of a profile within the reference length. The international ISO system defines this parameter as the difference in height between the average of the five highest peaks and the five lowest valleys along the profile.

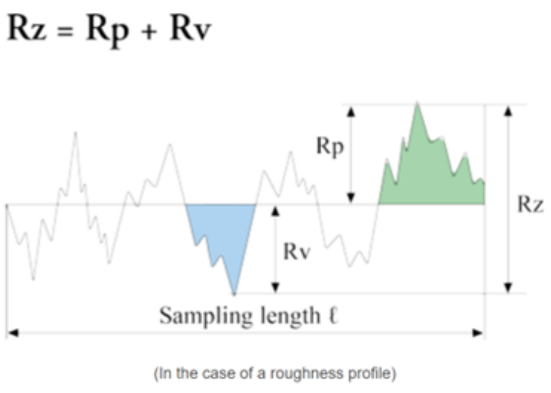

Figure 23: Rz parameter.

- Rsk (skewness) → the quotient of the mean cube value of Z(x) and the cube of R8 within a sampling length. It is the third central moment of the profile amplitude probability density function and is sensitive to occasional deep valleys or high peaks (in general, profiles with peaks removed or deep scratches have negative Rsk, while profiles with valleys filled in have positive Rsk). This parameter is also important in discriminating between surfaces that have different shapes but same Ra value.

  Rsk = 0: symmetric against the mean line (normal distribution)
  Rsk > 0: deviation beneath the mean line
  Rsk < 0: deviation above the mean line

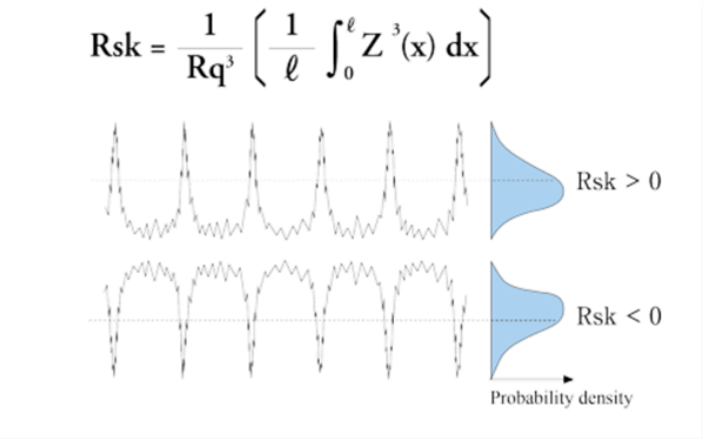

Figure 24: Rsk parameter.

- Rku (kurtosis) → the quotient of the mean quadratic value of Z(x) and the fourth power of Rq within a sampling length. This parameter is the fourth central moment of the profile amplitude probability density function and describes the sharpness of the probability density of the profile.

  Rku = 3: normal distribution
  Rku > 3: the height distribution is sharp (leptokurtoic, with relatively many high

peaks and low valleys)

Rku < 3: the height distribution is even (platykurtoic, with few high peaks and low valleys)

This parameter refers to the tip geometry of peaks and valleys and is suitable for analyzing the degree of contact between two objects.

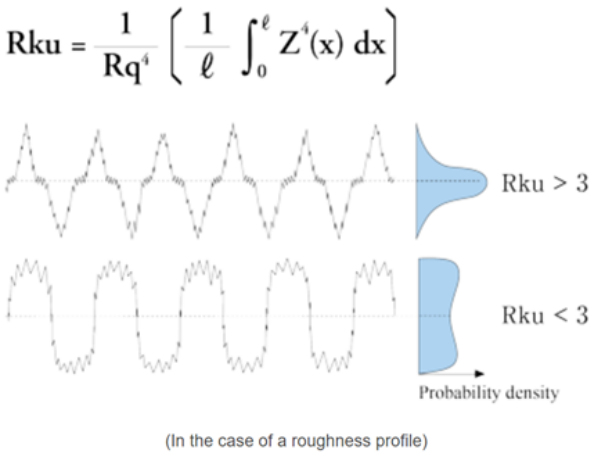

Figure 25: Rku parameter.

- Rk (core roughness depth) → represents the core height of the profile along the Y-axis of the BAC curve generated by placing a 40% line on the curve at the minimum slope point and extending the lines to 0%-100% points. This parameter is the depth of the roughness core profile.
- Rpk (reduced peak height) → represents the height of the Y-axis of a triangle with the same area as the BAC curve from 0% points to the Mr1 point. It is the mean height of the peaks protruding from the roughness core profile.
- Rvk (reduced valley depth) → represents the distance between the intersection line of the surface ratio Mr2 and the deepest valley. It is the mean depth of the valleys protruding from the roughness core profile.

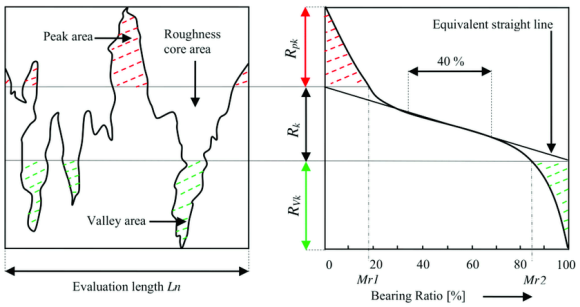

Figure 26: Rvk parameter.[21]

- Mr1 and Mr2 are the smallest and highest material ratios of the roughness core profile.

4.4. DIMENSIONAL PARAMETERS

For the extraction of geometrical parameters, in my study, I used both the software "MountainsMap" and "Python" [22, 23]. The use of "MountainsMap" was important for the values of the ball bearing starting from tactile measurements, the procedure is here explained:

a) Starting from the obtained profile (for tactile measurements) or profile extracted from a surface (for optical measurements), a level of the profile was done.

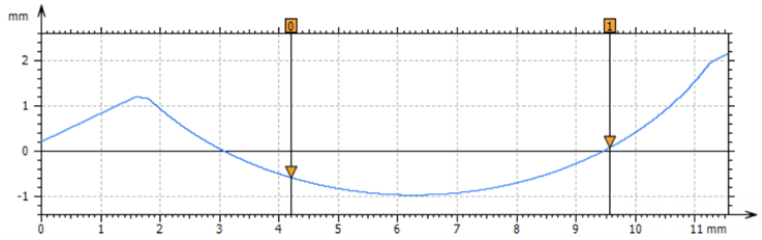

Figure 27: Ball bearing profile (circle).

b) Consequently, the extraction of an area can be done. In fact, in Figure 27 the profile of the ball bearing is represented, but the interesting area is only the middle one. The extraction of area was needed to obtain only the desired profile.

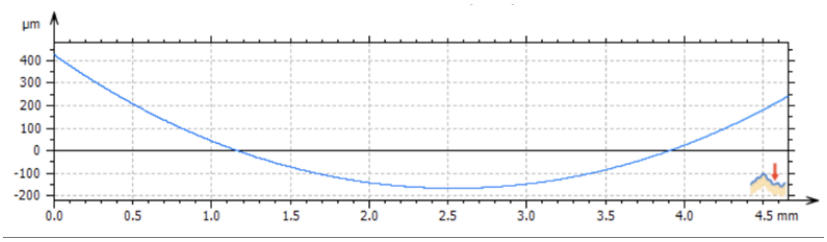

Figure 28: Extracted area of the ball bearing.

c) Subsequently, the "form removed" was performed to remove the form and obtain an isolated component that represents the curvature or deviation from a perfect circle, enhancing the accuracy of the final result.

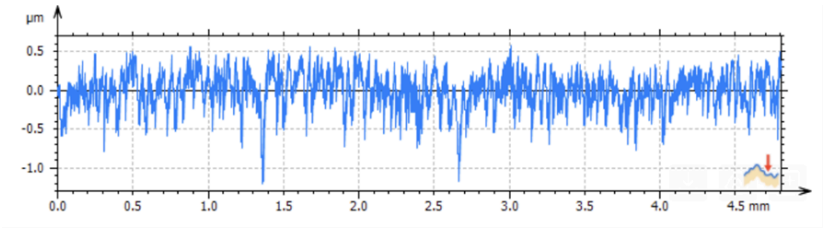

Figure 29: Form removed from ball bearing profile

d) The final step includes the calculation of the radius in the region that was chosen while extracting the area.

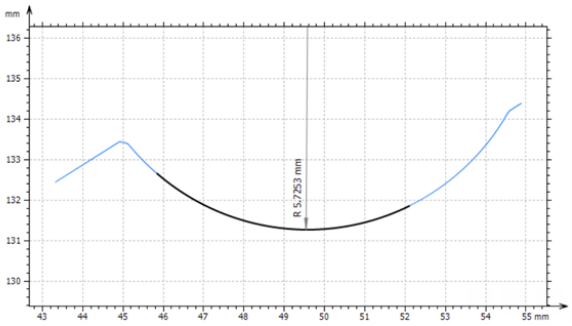

Figure 30: Radius calculation

Another method, utilized to calculate the radius from CCPS measurements, is the Least square Circle in Python. The program allows the removing of the best-fit circle from a topography. Furthermore, it also calculates the center position and the radius of the circle. The general equation of a circle is reported in Equation 2.

$$(x - x_c)^2 + (y - y_c)^2 = r^2 \tag{2}$$

Expanding the equation, we get Equation 3.

$$x^2 + y^2 = 2xx_c + 2yy_c + r^2 + x_c^2 + y_c^2 \tag{3}$$

Since we are interested in calculating the best r, x_c, y_c, that fit the measured points, we need to express the equation in matrix form according to Equation 4, Equation 5 and Equation 6.

$$f = \begin{pmatrix} x_i^2 + y_i^2 \\ \vdots \\ x_n^2 + y_n^2 \end{pmatrix} \tag{4}$$

$$A = \begin{pmatrix} 2x_i^2 & 2y_i^2 & 1 \\ \vdots & \vdots & \vdots \\ 2x_n^2 & 2y_n^2 & 1 \end{pmatrix} \tag{5}$$

$$c = \begin{pmatrix} x_c \\ y_c \\ r^2 - x_c^2 - y_c^2 \end{pmatrix} \tag{6}$$

We can now solve for c inverting the coefficients matrix A and find the best values for the four parameters of interest. The fit result is reported in the wireframe plot in Figure 31.

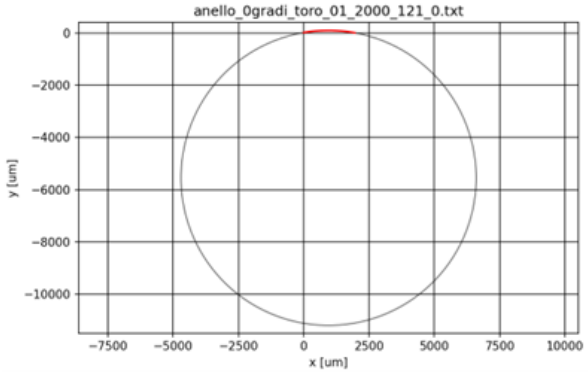

Figure 31: Fit of the least square circle.

4.5. GEAR TEETH

4.5.1. GEAR 801

Figure 32: Gear 801 measured by stylus profilometer.

Table 1 — *Roughness parameters for gear tooth 801, X direction*

	Stylus	**Confocal 20X**	**Confocal 50X**	**Interferometric 20X**	**Interferometric 50X**
Ra $[\mu m]$	0.20 ± 0.03	0.128 ± 0.008	0.213 ± 0.014	0.253 ± 0.001	0.213 ± 0.014
Rq $[\mu m]$	0.27 ± 0.04	0.173 ± 0.004	0.27 ± 0.02	0.0324 ± 0.0011	0.27 ± 0.02
Rz $[\mu m]$	1.07 ± 0.12	0.865 ± 0.03	2.8 ± 1.7	0.187 ± 0.005	2.8 ± 1.7
Rsk	-1.4 ± 0.5	-0.3 ± 0.4	-0.5 ± 0.6	-0.04 ± 0.13	-0.5 ± 0.6
Rku	8.3 ± 6.4	6.3 ± 1.9	9.3 ± 6.7	3.6 ± 0.2	9.32 ± 6.7
Rk $[\mu m]$	0.44 ± 0.07	0.37 ± 0.04	0.67 ± 0.04	0.078 ± 0.003	0.67 ± 0.04
Rpk $[\mu m]$	0.21 ± 0.04	0.19 ± 0.06	0.24 ± 0.06	0.032 ± 0.004	0.24 ± 0.06
Rvk $[\mu m]$	0.50 ± 0.05	0.235 ± 0.012	0.26 ± 0.07	0.036 ± 0.003	0.26 ± 0.07
Rmrk1 $[\%]$	10.6 ± 1.5	10.2 ± 1.0	10.1 ± 2.6	11.8 ± 1.2	10.1 ± 2.6
Rmrk2 $[\%]$	80.3 ± 1.5	87.2 ± 0.2	89.2 ± 1.9	90.0 ± 0.6	89.2 ± 1.9

Table 2 — *Roughness parameters for gear tooth 801, Y direction*

	Stylus	**Confocal 20X**	**Confocal 50X**	**Interferometric 20X**	**Interferometric 50X**
Ra $[\mu m]$	0.49 ± 0.04	0.42 ± 0.03	0.459 ± 0.009	-	-
Rq $[\mu m]$	0.63 ± 0.05	0.52 ± 0.02	0.619 ± 0.0014	-	-
Rz $[\mu m]$	3.5 ± 0.3	2.24 ± 0.10	6.44 ± 3.04	-	-
Rsk	-0.83 ± 0.07	-0.6 ± 0.2	-1.4 ± 0.5	-	-
Rku	4.4 ± 0.6	3.0 ± 0.5	11.1 ± 6.9	-	-
Rk $[\mu m]$	1.43 ± 0.13	1.35 ± 0.09	1.32 ± 0.06	-	-
Rpk $[\mu m]$	0.358 ± 0.076	0.17 ± 0.02	0.334 ± 0.007	-	-
Rvk $[\mu m]$	0.91 ± 0.11	0.64 ± 0.11	1.090 ± 0.004	-	-
Rmrk1 $[\%]$	8.3 ± 1.9	4.0 ± 0.7	10.0 ± 1.7	-	-
Rmrk2 $[\%]$	85.3 ± 1.9	86.5 ± 1.2	86.400.18	-	-

4.5.2. GEAR 825

A) 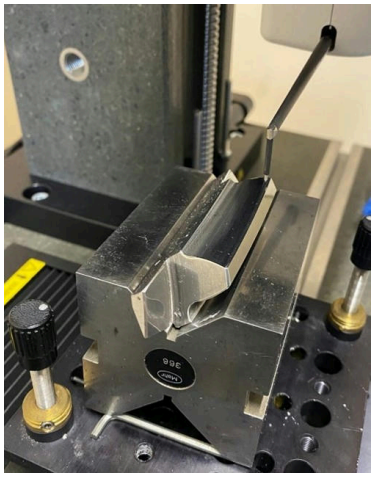 B) 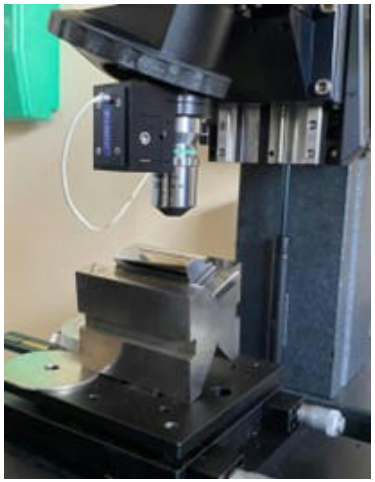

Figure 33: A) Gear 825 measured by stylus profilometer, B) Gear 825 measured by stylus profilometer.

Table 3 — *Roughness parameters for gear tooth 825, X direction*

	Stylus	**Confocal 20X**	**Confocal 50X**	**Interferometric 20X**	**Interferometric 50X**
Ra $[\mu m]$	0.0534 ± 0.0013	0.108 ± 0.003	0.070 ± 0.003	0.109 ± 0.003	0.070 ± 0.003
Rq $[\mu m]$	0.18 ± 0.03	0.1470 ± 0.0014	0.085 ± 0.004	0.0142 ± 0.0004	0.085 ± 0.004
Rz $[\mu m]$	0.59 ± 0.03	0.676 ± 0.06	0.54 ± 0.08	0.072 ± 0.004	0.54 ± 0.08
Rsk	-11.6 ± 0.8	-1.3 ± 0.4	-0.234 ± 0.2	3.9 ± 0.5	-0.234 ± 0.2
Rku	186 ± 15.3	6.6 ± 1.2	3.0 ± 0.5	-0.365 ± 0.15	3.0 ± 0.5
Rk $[\mu m]$	0.079 ± 0.010	0.29 ± 0.03	0.246 ± 0.003	0.029 ± 0.002	0.078 ± 0.018
Rpk $[\mu m]$	0.18 ± 0.05	0.101 ± 0.010	0.056 ± 0.013	0.0154 ± 0.0004	0.022 ± 0.004
Rvk $[\mu m]$	0.266 ± 0.008	0.252 ± 0.008	$0.080 \pm 0.0150.10$	0.01780 ± 0.00004	± 0.03
Rmrk1 $[\%]$	10.5 ± 0.4	7.8 ± 0.4	5.3 ± 2.0	12.7 ± 0.7	8.1 ± 0.9
Rmrk2 $[\%]$	85.0 ± 1.0	84.3 ± 1.6	92.20 ± 2.05	84.5 ± 2.2	83.9 ± 1.6

Table 4 — *Roughness parameters for gear tooth 825, Y direction*

	Stylus	**Confocal 20X**	**Confocal 50X**	**Interferometric 20X**	**Interferometric 50X**
Ra $[\mu m]$	0.05 ± 0.02	0.082 ± 0.007	0.050 ± 0.001	-	-
Rq $[\mu m]$	0.09 ± 0.07	0.112 ± 0.011	0.062 ± 0.001	-	-
Rz $[\mu m]$	1.01 ± 0.4	0.667 ± 0.05	0.319 ± 0.014	-	-
Rsk	-2.7 ± 2.9	-1.23 ± 0.05	-0.19 ± 0.12	-	-
Rku	34.1 ± 31.6	7.0 ± 0.5	2.48 ± 0.08	-	-
Rk $[\mu m]$	0.13 ± 0.02	0.2290 ± 0.012	0.142 ± 0.002	-	-
Rpk $[\mu m]$	0.07 ± 0.05	0.09 ± 0.02	0.046 ± 0.005	-	-
Rvk $[\mu m]$	0.15 ± 0.17	0.19 ± 0.02	0.061 ± 0.002	-	-
Rmrk1 $[\%]$	15.0 ± 5.3	7.9 ± 0.6	12.10 ± 4.06	-	-
Rmrk2 $[\%]$	89.8 ± 3.4	86.1 ± 0.3	82.90 ± 2.09	-	-

4.6. BALL BEARING

A) 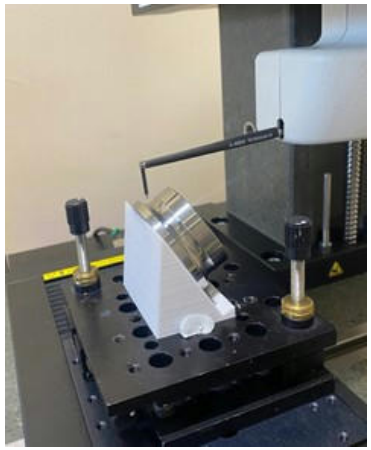

B) 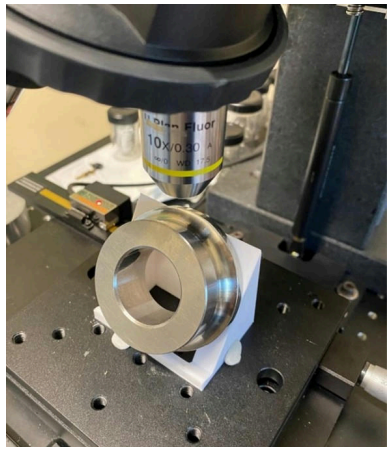

C) 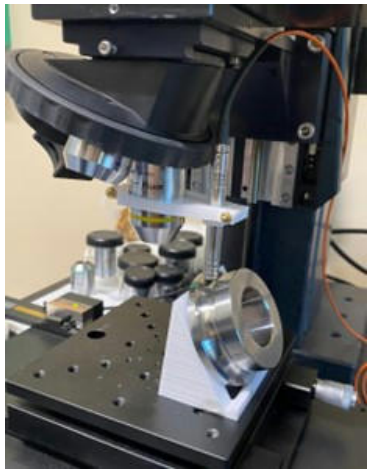

D) 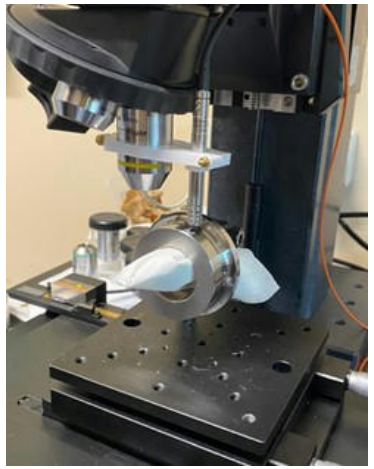

Figure 34: A) Ball bearing measured by stylus profilometer, B) Ball bearing measured by optical profilometer, C) Ball bearing circle measured by CCPS, D) Ball bearing torus measured by CCPS.

Table 5 — *Roughness parameters for ball bearing circle.*

	Stylus	Confocal 20X	Confocal 50X	Interferometric 20X	Interferometric 50X
Ra $[\mu m]$	0.16 ± 0.03	0.062 ± 0.017	0.14 ± 0.04	–	–
Rq $[\mu m]$	-0.8 ± 0.3	0.08 ± 0.02	0.20 ± 0.05	–	–
Rz $[\mu m]$	4.4 ± 0.8	0.42 ± 0.16	1.5 ± 0.6	–	–
Rsk	0.69 ± 0.16	-0.22 ± 1.02	0.3 ± 0.7	–	–
Rku	0.12 ± 0.03	4.4 ± 3.4	6.1 ± 2.2	–	–
Rk $[\mu m]$	0.34 ± 0.09	0.18 ± 0.06	0.33 ± 0.10	–	–
Rpk $[\mu m]$	0.11 ± 0.02	0.08 ± 0.04	0.33 ± 0.09	–	–
Rvk $[\mu m]$	0.24 ± 0.06	0.09 ± 0.04	0.25 ± 0.14	–	–
Rmrk1 $[\%]$	8.82 ± 1.11	9.1 ± 1.9	11.8 ± 10.06	–	–
Rmrk2 $[\%]$	84.6 ± 1.3	86.4 ± 2.9	83.8 ± 8.2	–	–

Table 6 — *Roughness parameters for ball bearing torus.*

	Stylus	Confocal 20X	Confocal 50X	Interferometric 20X	Interferometric 50X
Ra $[\mu m]$	0.159 ± 0.004	1.06 ± 0.09	0.16 ± 0.03	0.26 ± 0.04	0.17 ± 0.03
Rq $[\mu m]$	0.204 ± 0.005	1.5 ± 0.19	-0.8 ± 0.3	-0.78 ± 0.13	0.24 ± 0.05
Rz $[\mu m]$	1.09 ± 0.06	9.7 ± 1.5	4.4 ± 0.8	4.7 ± 0.9	1.6 ± 0.6
Rsk	-0.79 ± 0.13	1.8 ± 1.3	0.69 ± 0.16	1.7 ± 0.2	-1.8 ± 3.0
Rku	4.6 ± 0.9	11.1 ± 10.6	0.12 ± 0.03	0.20 ± 0.03	33.3 ± 57.8
Rk $[\mu m]$	0.48 ± 0.02	2.65 ± 0.16	0.34 ± 0.09	0.56 ± 0.07	0.47 ± 0.15
Rpk $[\mu m]$	0.12 ± 0.02	2.9 ± 0.8	0.11 ± 0.02	0.19 ± 0.08	0.25 ± 0.08
Rvk $[\mu m]$	0.29 ± 0.02	0.8 ± 0.3	0.24 ± 0.06	0.40 ± 0.10	0.34 ± 0.06
Rmrk1 $[\%]$	7.4 ± 1.4	16.9 ± 1.4	8.82 ± 1.11	9.0 ± 3.3	9.28 ± 1.09
Rmrk2 $[\%]$	86.2 ± 1.4	92.3 ± 1.5	84.6 ± 1.3	85.5 ± 3.4	84.8 ± 4.5

Table 7 — *Calculated radius for the ball bearing circle.*

	Value from technical drawing		**stylus**	**CCPS**
Radius $[mm]$	26.10	**Radius** $[mm]$	25.9	26.104
Tolerance $[mm]$	0.01	**St Dev** $[mm]$	2.4	0.006

Table 8 — *Calculated radius for the ball bearing torus.*

	Value from technical drawing		**stylus**	**CCPS**
Radius $[mm]$	5.737	**Radius** $[mm]$	5.73	5.730
Tolerance $[mm]$	0.007	**St Dev** $[mm]$	0.01	0.003

4.7. LARGE RING SEGMENT

A) 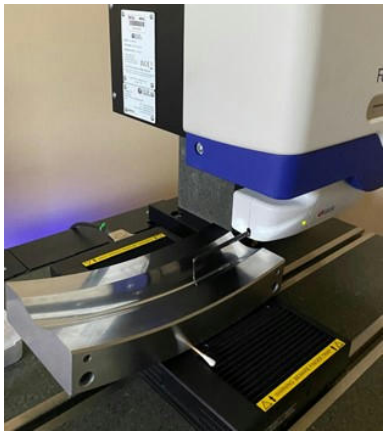 B)  C) 

Figure 35: A) Large ring section measured by stylus profilometer, B) Large ring section measured by optical profilometer, C) Large ring section measured by CCPS, D) Ball bearing torus measured by CCPS.

Table 9 — *Roughness parameters for large ring segment, right side, 0 degree.*

	Stylus	**Confocal 20X**	**Confocal 50X**	**Interferometric 20X**	**Interferometric 50X**
Ra $[\mu m]$	0.02510 ± 0.00005	0.046 ± 0.002	0.0205 ± 0.0014	$[0.0195 \pm 0.0015$	0.027 ± 0.002
Rq $[\mu m]$	0.03570 ± 0.00003	0.0567 ± 0.005	0.0257 ± 0.002	0.0264 ± 0.002	0.0444 ± 0.004
Rz $[\mu m]$	0.185 ± 0.002	0.25 ± 0.02	0.120 ± 0.006	0.14 ± 0.02	0.172 ± 0.012
Rsk	1.11 ± 0.05	-0.06 ± 0.03	0.36 ± 0.02	0.69 ± 0.18	3.5 ± 0.4
Rku	6.5 ± 0.3	2.9 ± 0.5	2.97 ± 0.08	4.6 ± 0.5	20.2 ± 3.5
Rk $[\mu m]$	0.0652 ± 0.0002	0.128 ± 0.010	0.06 ± 0.002	0.053 ± 0.003	0.070 ± 0.004
Rpk $[\mu m]$	0.0732 ± 0.0009	0.060 ± 0.008	0.031 ± 0.004	0.047 ± 0.008	0.12 ± 0.02
Rvk $[\mu m]$	0.0315 ± 0.0009	0.059 ± 0.007	0.020 ± 0.001	0.025 ± 0.003	0.009 ± 0.002
Rmrk1 $[\%]$	13.8 ± 0.03	9.5 ± 2.5	15.30 ± 1.12	11.9 ± 0.3	11.4 ± 2.5
Rmrk2 $[\%]$	89.9 ± 0.4	84.4 ± 3.6	91.5 ± 0.5	86.5 ± 0.9	95.7 ± 2.6

Table 10 — *Roughness parameters for large ring segment, left side, 0 degree.*

	Stylus	Confocal 20X	Confocal 50X	Interferometric 20X	Interferometric 50X
Ra $[\mu m]$	0.04620 ± 0.00004	0.050 ± 0.009	0.040 ± 0.005	—	—
Rq $[\mu m]$	0.1020 ± 0.0002	0.0648 ± 0.009	0.050 ± 0.003	—	—
Rz $[\mu m]$	0.3280 ± 0.0016	0.33 ± 0.03	0.234 ± 0.003	—	—
Rsk	-9.28 ± 0.13	-0.39 ± 0.17	0.8 ± 0.4	—	—
Rku	155.0 ± 3.5	3.9 ± 0.8	3.3 ± 1.0	—	—
Rk $[\mu m]$	0.104 ± 0.003	0.14 ± 0.03	0.11 ± 0.02	—	—
Rpk $[\mu m]$	0.1140 ± 0.0017	0.070 ± 0.016	0.073 ± 0.017	—	—
Rvk $[\mu m]$	0.157 ± 0.003	0.085 ± 0.005	0.022 ± 0.001	—	—
Rmrk1 $[\%]$	16.5 ± 0.8	10.90 ± 3.07	19.70 ± 0.75	—	—
Rmrk2 $[\%]$	90.9 ± 0.2	85.9 ± 2.7	93.90 ± 0.81	—	

Table 11 — *Roughness parameters for large ring segment, center, 0 degree.*

	Stylus	Confocal 20X	Confocal 50X	Interferometric 20X	Interferometric 50X
Ra $[\mu m]$	0.03010 ± 0.00013	0.050 ± 0.009	0.038 ± 0.004	0.0176 ± 0.0010	0.027 ± 0.004
Rq $[\mu m]$	0.03980 ± 0.00012	0.0648 ± 0.009	0.0491 ± 0.005	0.0219 ± 0.0013	0.0649 ± 0.003
Rz $[\mu m]$	0.1980 ± 0.0003	0.33 ± 0.03	0.299 ± 0.003	0.124 ± 0.003	0.21 ± 0.02
Rsk	0.753 ± 0.010	-0.39 ± 0.17	0.3 ± 0.3	0.30 ± 0.12	9.2 ± 0.4
Rku	4.55 ± 0.06	3.9 ± 0.8	4.4 ± 0.2	3.08 ± 0.08	114.0 ± 7.7
Rk $[\mu m]$	0.0857 ± 0.0007	0.14 ± 0.038	0.108 ± 0.005	0.057 ± 0.002	0.06 ± 0.02
Rpk $[\mu m]$	0.0633 ± 0.0001	0.070 ± 0.016	0.066 ± 0.015	0.024 ± 0.004	0.071 ± 0.005
Rvk $[\mu m]$	0.0296 ± 0.0002	0.085 ± 0.005	0.0441 ± 0.0005	0.0159 ± 0.0004	0.072 ± 0.002
Rmrk1 $[\%]$	13.60 ± 0.08	10.90 ± 3.07	13.1 ± 2.0	10.8 ± 1.3	20.0 ± 0.4
Rmrk2 $[\%]$	89.6 ± 0.2	85.9 ± 2.7	89.6 ± 0.2	92.5 ± 0.8	93.2 ± 1.5

Table 12 — *Roughness parameters for large ring segment, right side, 90 degree.*

	Stylus	Confocal 20X	Confocal 50X	Interferometric 20X	Interferometric 50X
Ra $[\mu m]$	0.071 ± 0.004	0.122 ± 0.007	0.0554 ± 0.0011	0.081 ± 0.005	0.063 ± 0.011
Rq $[\mu m]$	0.092 ± 0.003	0.163 ± 0.008	0.0958 ± 0.004	0.103 ± 0.006	0.079 ± 0.02
Rz $[\mu m]$	0.549 ± 0.008	1.03 ± 0.03	0.56 ± 0.01	0.51 ± 0.03	0.39 ± 0.06
Rsk	-0.9 ± 0.2	-1.01 ± 0.06	5.6 ± 0.4	-0.88 ± 0.06	-0.6 ± 0.4
Rku	5.23 ± 1.05	8.6 ± 2.2	63.2 ± 5.5	3.58 ± 0.11	3.2 ± 0.5
Rk $[\mu m]$	0.21 ± 0.02	0.363 ± 0.011	0.159 ± 0.003	0.233 ± 0.004	0.184 ± 0.010
Rpk $[\mu m]$	0.065 ± 0.003	0.127 ± 0.002	0.170 ± 0.004	0.040 ± 0.003	0.038 ± 0.009
Rvk $[\mu m]$	0.135 ± 0.008	0.24 ± 0.02	0.077 ± 0.003	0.163 ± 0.016	0.12 ± 0.06
Rmrk1 $[\%]$	8.0 ± 0.5	9.1 ± 0.4	7.4 ± 0.8	3.8 ± 0.4	5.5 ± 1.6
Rmrk2 $[\%]$	85.7 ± 0.7	87.1 ± 1.1	86.4 ± 0.5	83.5 ± 1.4	85.4 ± 3.8

Table 13 — Roughness parameters for large ring segment, left side, 90 degree

	Stylus	Confocal 20X	Confocal 50X	Interferometric 20X	Interferometric 50X
Ra $[\mu m]$	0.0979 ± 0.0001	0.235 ± 0.007	0.097 ± 0.001	0.115 ± 0.004	0.108 ± 0.004
Rq $[\mu m]$	0.1260 ± 0.0001	0.295 ± 0.009	0.123 ± 0.002	0.157 ± 0.005	0.13 ± 0.004
Rz $[\mu m]$	0.707 ± 0.003	1.53 ± 0.07	0.58 ± 0.02	1.030 ± 0.008	0.59 ± 0.02
Rsk	-0.618 ± 0.004	-0.74 ± 0.01	0.02 ± 0.04	-4.6 ± 0.3	-0.014 ± 0.012
Rku	4.000 ± 0.016	3.47 ± 0.06	3.220 ± 0.0011	108.0 ± 11.9	2.40 ± 0.04
Rk $[\mu m]$	0.2980 ± 0.0005	0.67 ± 0.02	0.297 ± 0.001	0.333 ± 0.004	0.361 ± 0.008
Rpk $[\mu m]$	0.08430 ± 0.00013	0.15 ± 0.03	0.133 ± 0.004	0.093 ± 0.006	0.103 ± 0.011
Rvk $[\mu m]$	0.1710 ± 0.0005	0.43 ± 0.03	0.125 ± 0.004	0.225 ± 0.010	0.091 ± 0.007
Rmrk1 $[\%]$	9.20 ± 0.08	5.7 ± 0.4	9.2 ± 0.5	6.1 ± 0.4	7.4 ± 0.8
Rmrk2 $[\%]$	87.10 ± 0.01	83.2 ± 1.3	87.2 ± 0.4	85.2 ± 1.1	90.20 ± 0.03

Table 14 — *Roughness parameters for large ring segment, center, 90 degree.*

	Stylus	Confocal 20X	Confocal 50X	Interferometric 20X	Interferometric 50X
Ra $[\mu m]$	0.0890 ± 0.0003	0.191 ± 0.010	0.11 ± 0.02	0.1180 ± 0.0013	0.072 ± 0.010
Rq $[\mu m]$	0.164 ± 0.002	0.31 ± 0.02	0.14 ± 0.02	0.305 ± 0.003	0.0891 ± 0.011
Rz $[\mu m]$	0.790 ± 0.002	2.6 ± 0.5	0.86 ± 0.12	1.00 ± 0.10	0.454 ± 0.011
Rsk	1.2 ± 0.4	7.0 ± 2.3	-0.4 ± 0.3	10.7 ± 0.2	-0.3 ± 0.2
Rku	75.2 ± 2.4	237.0 ± 66.7	4.06 ± 0.03	161.0 ± 4.2	3.2 ± 0.6
Rk $[\mu m]$	0.2240 ± 0.0003	0.55 ± 0.02	0.31 ± 0.04	0.285 ± 0.013	0.24 ± 0.04
Rpk $[\mu m]$	0.193 ± 0.002	0.287 ± 0.016	0.104 ± 0.015	0.47 ± 0.10	0.067 ± 0.010
Rvk $[\mu m]$	0.205 ± 0.003	0.46 ± 0.13	0.17 ± 0.06	0.27 ± 0.02	0.091 ± 0.010
Rmrk1 $[\%]$	9.30 ± 0.03	9.1 ± 1.6	8.2 ± 1.3	9.8 ± 3.4	8.2 ± 0.5
Rmrk2 $[\%]$	84.70 ± 0.06	88.30 ± 0.14	85.4 ± 2.0	87.1 ± 0.2	90.4 ± 0.5

Table 15 — *Calculated radius for the large ring segment 0 degree.*

	Value from technical drawing		stylus	CCPS
Radius $[mm]$	44.0820	**Radius** $[mm]$	44.01	44.011
Tolerance $[mm]$	0.0016	**St Dev** $[mm]$	0.07	0.003

Table 16 — *Calculated radius for the large ring segment 90 degree.*

	Value from technical drawing		stylus	CCPS
Radius $[mm]$	26.10	**Radius** $[mm]$	25.9	26.104
Tolerance $[mm]$	0.01	**St Dev** $[mm]$	2.4	0.006

5. COMPARISON

Since optical measuring systems are widespread in surface and coordinate metrology as they are fast, with high resolution, and contactless, an intercomparison between contact and non-contact measurements is done. There are several European projects (*e.g.* TracOptic [24]) which aim to improve the traceability of 3D roughness and dimensional measurements using optical 3D microscopy and optical distance sensors. Optical measurements are essential for the factory of the future and are indispensable nowadays in industry. One challenge is that the traceability is more complex than for tactile instruments.

The stylus profilometer measurements are taken as a reference, because the results obtained by this technique are the most stable and accurate. In a previous work, performed in the first month of my thesis [1], the Taylor Hobson TalySurf PGI Novus S10 has been metrologically characterized, calibrated and traced to the International System of Units (SI). Considering the optical methods:

a) The optical profilometer, both in confocal and interferometric modalities allows to measure areal topographies, and in order to compare results with stylus profilometer profiles are extracted from images. For roughness analysis a 50X objective was used.
b) CCPS is an optical and not-contact method which is used only for performing form measurements, because it is coupled with the Z motion axis of the optical profilometer, which has a linear encoder with a resolution of 100 nm, limiting the CCPS capability to resolve lower roughness profiles.

In my study an intercomparison between stylus profilometer and optical profilometer was done for the roughness parameters, while a comparison between stylus profilometer and CCPS was done for calculating the radius.

In particular, considering the roughness parameters reported in my study, the main focus was on the most used parameter, Ra, which is the arithmetic mean deviation, and represents the average roughness of a surface and is a key indicator of surface finish quality. It helps in determining how smooth or rough a surface is, which can affect the functionality, appearance, and wear resistance of the material.

Using a CCPS to perform form measurements offers significant advantages over traditional contact-based coordinate measuring machines (CMMs). The non-contact nature of the optical probe prevents sample damage and allows for significantly reduced sampling spacing (40 points/mm), enhancing measurement precision and enabling the detailed capture of freeform surfaces.

As it is possible to see in Section 4.5, the geometry information is not present since the mathematics behind the gears is very complex and it needs further investigations that will be carried

out in the future. Indeed, considering the mathematics behind gears is extraordinarily complex and its analysis has not been carried out in this study.

Table 7 highlights a discrepancy in the radius values obtained from the stylus profilometer and the CCPS. This difference can be attributed to the tactile method employed, which involved conducting the measurement on a support inclined at 30°. This inclination introduces a potential source of error, potentially leading to a misleading result in the stylus measurements.

In the remaining tables, the measurements taken with the stylus profilometer and the optical profilometer show a consistent agreement with each other. This demonstrates that both optical and contact techniques can be considered reliable for obtaining accurate surface measurements. The concordance between these two methods underscores the reliability of both techniques, confirming that they can be effectively used in tandem for comprehensive surface analysis.

Another important consideration for objectives (optical profilometer) is about the correlation between Numerical Aperture (NA), light propagation and Working Distance (WD). In fact, increasing the NA corresponds to an increased light and a decreased WD. This is also the reason why in some tables, such as Table 5, was not possible to obtain data for the interferometric profilometer since the WD was too low.

Conclusion

In this study three different mechanical components employed in systems for energy harvesting, each with distinct three surface treatments, were analyzed to determine their roughness and dimensional parameters.

The data revealed that the large ring section exhibits the lowest roughness (Ra = 0.0338 ± 0.00015 μm) [3], which is in accordance with the fact that this element has a high resemblance to actual wind turbines components. Its low roughness it is also attributed to its complex processing, as detailed in Section 2.3.

Hence, considering the materials science field it was also possible to observe that the direction of analysis strongly influences the final results. In particular, the roughness parameters vary depending on the orientation of the measurements, highlighting the presence of a preferential direction in the surface processing also due to its application requirements, such as the ball sliding (very important for the large segment ring).

Moreover, considering the metrological objectives, a tactile technique was used as reference as this instrument is traceable to the International System of Unit (SI), and it has been calibrated during the first month of my internship. On the contrary, employing non-contact methods offer advantages since they do not necessitate direct contact with the surface reducing the risk of physical damages, however these non-contact techniques lack traceability due to light-surface interactions. Therefore, comparisons between different methods are needed to assess the reliability of optical measurements, with the goal of carrying out future research to make non-contact techniques traceable.

The uncertainty budgets are not addressed in this study as they will be examined and explored in depth in following studies.

In conclusion, my work focused on analyzing different parameters, such as roughness and dimensional characteristics, to understand the relationship between the surface properties and the functionality and overall efficiency of energy harvesting systems.

---

[3] This value has been obtained from an average of the roughness parameter Ra for the large ring segment, by averaging the results and averaging the standard deviations associated using the formula:

$$\text{mean of standard deviation} = \sqrt{(SD_1)^2 + ... + (SD_2)^2} \tag{7}$$

References

[1] Luigi Ribotta, Elisa Destefano, Anas Guendouli, Andrea Giura, Roberto Bellotti, Massimo Zucco, *Metrological Confirmation of the Stylus Profilometer Taylor Hobson Form Talysurf PGI Novus S 10*, 2024, TR 14/2024, Accessed: 2024-06-11. Retrieved from https://iris.inrim.it/handle/11696/80999

[2] Tan, Dr. Özgür, *Overview of optical methods for surface metrology*. Retrieved June 11, 2024 from https://magazine.polytec.com/int/overview-of-optical-methods-for-surface-metrology

[3] Emma Haynes, David Knowles, *Advanced materials metrology strategy*, 2024, National Physical Laboratory (NPL).

[4] Bellotti Roberto, Maras Claire, Picotto Gian Bartolo, Pomeretto Marco, Ribotta Luigi, *3D characterization of printed structures by stylus and optical based measurements*, 2018, 18Th international conference of European society for precision engineering and nanotechnology.

[5] Wenjuan Sun, Andrew J Lancaster and Claudiu L. Giusca, *Surface texture measurements of gear surface using stylus instruments*, 2017, NPL Management Limited, ISBN: 1368-6550.

[6] Ye, Ronan, *What is grinding: definition, process, types and specifications*, 2024. Retrieved May 15, 2024 from https://www.3erp.com/blog/what-is-grinding/

[7] Matthew Wagner, Mark Michaud, Aaron Isaacson and Bell, Matt, *A comparison of surface roughness measurement methods for gear tooth working surface*, 2019, AGMA, Fall Technical Meeting, EUSPEN.

[8] Shivashankara, Mahadev Gowda Patil, Rudra Naik, *Evaluation of vitrified bonding strength using aluminum oxide with boron nitride grinding wheel*, 2023, Materials Today: Proceedings 92, 271–277.

[9] Gimpert, Adam, *An introduction to the hard finishing of gears*, 2016. Retrieved May 4, 2024 from https://asthegearturns.com/2016/06/22/hard-finishing-gears-part-1/

[10] Cieniek, Łukasz, *Surface engineering course held in AGH University of Science and Technology*, 2024.

[11] Gülcan Toktaş, Alaaddin Toktaş, Murat Can Dura, *Investigating the wear behavior of induction hardened 100Cr6 steel*, 2023, Sakarya University journal of Science 22, 1174–1180. https://doi.org/10.16984/saufenbilder.304203

[12] Sompoliński, Virgamet Piotr, *High-carbon bearing steel 100cr6, 1.3505 and tool steel 102cr6, 1.2067 abrasion resistive, for rolling-contact bearings according to iso 4957 and iso 683-17*, 2018. Retrieved April 8, 2024 from https://virgamet.com/tubes-100cr6-1-3505-102cr6-1-2067-aisi-52100-lh15-bearing-steel

[13] Alessandro Balsamo, Gian Bartolo Picotto, Davide Corona, Roberto Frizza, *Design, manufacturing and calibration of a large ring segment*, 2019, 16th International Conference of the European Society for Precision Engineering and Nanotechnology.

[14] Limited, Taylor Hobson, *Exploring Surface Texture: A fundamental guide to the measurement of surface finish*, 2003, 7th edition. https://doi.org/10.1007/978-3-642-36458-7

[15] Clement Moreau, Maxence Bigerelle, Julie Marteau, Julie Lemesle, David Perez, Robin Guibert, François Blateyron and Christopher A Brown, *A novel methodology to assess optical profilometer stability to discriminate surface roughness*, 2024, Surface Topography Metrology and Propertiese. https://doi.org/10.1088/2015-672X/ad4378

[16] Blateyron, François, *Good practices for the use of areal filters*, Retrived June 2024 from https://www.digitalsurf.com/en/guide.html.

[17] Leach, Richard, *Characterization of Areal Surface Texture*, 2013. https://doi.org/10.1007/978-3-642-36458-7

[18] *Surface roughness and parameters*. Retrieved May 20, 2024 from https://www.predev.com/pdffiles/surface_roughness_terminology_and_parameters.pdf

[19] S. Gadelmawla, T.M.A. Maksoud , I.M. Elewa , H.H. Soliman, M.M. Koura, *Roughness parameters*, 2002, Journal of Materials processing Technology 123, 133–145. https://doi.org/10.1016/S0924-0136(02)00060-2

[20] *Surface Roughness Measurement – Parameters*. Retrieved April 23, 2024 from https://www.olympus-ims.com/en/metrology/surface-roughness-measurement-portal/parameters/

[21] Amine Hamdi, Toufik Aliouane, Sidi Mohammed Merghache, *Effect of cutting variables on bearing area curve parameters (BAC-P) during hard turning process*, 2020, Archieve of mechanical engineering 67,. https://doi.org/10.24425/ame.2020.131684

[22] Kenichi Kanatani, Prasanna Rangarajan, *Hyper least squares fitting of circles and ellipses*, 2011.

[23] Rangarajan, Kenichi & Niitsuma, Hirotaka & Sugaya, Yasuyuki, Prasanna & Kanatani, *Hyper Least Squares and Its Applications*, 2010, 5–8. https://doi.org/10.1109/ICPR.2010.10

[24] *TracOptic*. Retrieved June 19, 2024 from https://www.ptb.de/empir2021/tracoptic/project/overview/

,